Fe-Substitution for Ni in Misch Metal-Based Superlattice Hydrogen Absorbing Alloys—Part 1. Structural, Hydrogen Storage, and Electrochemical Properties

Kwo-Hsiung Young [1,2,*], Taihei Ouchi [2], Jean Nei [2] and Shigekazu Yasuoka [3]

[1] Department of Chemical Engineering and Materials Science, Wayne State University, Detroit, MI 48202, USA

[2] BASF/Battery Materials-Ovonic, 2983 Waterview Drive, Rochester Hills, MI 48309, USA; taihei.ouchi@basf.com (T.O.); jean.nei@basf.com (J.N.)

[3] Engineering Division, Ni-MH Group, FDK Corporation, 307-2, Koyagi-Machi, Takasaki, Gunma 370-0042, Japan; shigekazu.yasuoka@fdk.co.jp

* Correspondence: kwo.young@basf.com; Tel.: +1-248-293-7000

Abstract: The effects of Fe partially replacing Ni in a misch metal-based superlattice hydrogen absorbing alloy (HAA) were studied. Addition of Fe increases the lattice constants and abundance of the main Ce_2Ni_7 phase, decreases the $NdNi_3$ phase abundance, and increases the $CaCu_5$ phase when the Fe content is above 2.3 at%. For the gaseous phase hydrogen storage (H-storage), Fe incorporation does not change the storage capacity or equilibrium pressure, but it does decrease the change in both entropy and enthalpy. With regard to electrochemistry, >2.3 at% Fe decreases both the full and high-rate discharge capacities due to the deterioration in both bulk transport (caused by decreased secondary phase abundance and consequent lower synergetic effect) and surface electrochemical reaction (caused by the lower volume of the surface metallic Ni inclusions). In a low-temperature environment (-40 °C), although Fe increases the reactive surface area, it also severely hinders the ability of the surface catalytic, leading to a net increase in surface charge-transfer resistance. Even though Fe increases the abundance of the beneficial Ce_2Ni_7 phase with a trade-off for the relatively unfavorable $NdNi_3$ phase, it also deteriorates the electrochemical performance due to a less active surface. Therefore, further surface treatment methods that are able to increase the surface catalytic ability in Fe-containing superlattice alloys and potentially reveal the positive contributions that Fe provides structurally are worth investigating in the future.

Keywords: metal hydride (MH); nickel/metal hydride (Ni/MH) battery; hydrogen absorbing alloy (HAA); electrochemistry; superlattice alloy

1. Introduction

Misch metal-based superlattice hydrogen absorbing alloy (HAA) has become the mainstream negative electrode active material for commercial nickel/metal hydride (Ni/MH) batteries due to its higher capacity, improved high-rate capability, wider operating temperature range, and lower self-discharge compared to the conventional AB_5 HAA [1–4]. Superlattice HAAs belong to a family of alloys mainly composed of AB_3, A_2B_7, and A_5B_{19} structures, which are constructed with various numbers of AB_5 building slabs (one, two, and three, respectively) between the A_2B_4 building slabs [5–7]. Other non-superlattice phases, such as AB_2, $MgLaNi_4$, and AB_5, may also be present in these multi-phase superlattice alloys [8–11]. While the basic formula of the commercial superlattice HAAs contains only rare earth metals (La, Pr, Nd, and/or Sm), Ni, or Al, we have previously reported

the effects of adding Ce [12], Mn [8,13], and Co [9,14]. In general, Ce promotes AB_2 phase formation and deteriorates battery performance, Mn improves the high-rate performance but creates micro-shorts in the separator and consequently causes severe self-discharge, and Co improves the low-temperature performance with the sacrifices in self-discharge and high-temperature performance. In this paper, we investigate the effects of Fe, another transition metal with an atomic number between Mn and Co, partially replacing Ni on the structural, gaseous phase storage, and electrochemical properties of HAA.

Fe has been used as a low-cost supplement in AB_2 [15–22], AB_5 [23–34], and body-centered-cubic (bcc) [35–40] HAAs. However, the results of Fe incorporation in these HAAs have so far been inconsistent. For example, the addition of Fe to V-containing AB_2 HAA deteriorated the low-temperature performance but increased the discharge capacity [21] and cycle stability [18]. Contradictory results from adding Fe to V-free AB_2 HAA were also reported (improved low-temperature performance but degraded capacity and cycle performance) [22]. Moreover, Fe incorporation in AB_5 HAA enhanced the low-temperature performance due to increases in surface area [23,28] and surface catalytic ability [34], but lowered the capacity [23,27,28,34] and cycle stability [29,34]. However, negative impact on low-temperature performance [30] and positive contribution to cycle stability [32] from Fe addition in AB_5 HAA have also been previously reported. In the Laves phase-related bcc solid solution HAA, Fe impeded high-rate dischargeability (HRD) [40] and decreased the bcc phase abundance [35,36], but the opposite results have also been reported (improved HRD and increased bcc phase abundance) [37]. In addition, ferrovanadium was used as an alternative and inexpensive source of vanadium in the bcc HAA [38,39]. Very few results regarding Fe addition in the superlattice HAA have been published, and all published articles concerned the La-only alloy, which has very limited use in practical Ni/MH battery applications due to its easily oxidized nature and thus short life cycle [41]. Wang et al. [42] reported that Fe addition in the $(La,Mg)Co_{0.45}Ni_{2.55}$ HAA decreased the discharge capacity and HRD, but improved the charge stability. Wu et al. [43] reported that Fe substitution in the $La_{0.7}Ng_{0.3}Ni_3$ superlattice HAA resulted in a lower capacity and HRD. Since any investigation on the effects of Fe incorporation in the misch metal-based superlattice HAA was absent, such results are very desirable in order to further improve the electrochemical properties of the superlattice HAA. While this paper (Part 1) summarizes the results of structural, gaseous phase, and electrochemical (in half-cell configuration) studies on the Fe-substituted misch metal-based superlattice alloys, the performance and failure analysis of the Ni/MH batteries made using these alloys will be discussed in another publication (Part 2, [44]).

2. Experimental Setup

First, −200 mesh HAA powder (2 kg per composition) was prepared by Japan Metals & Chemicals Company (Tokyo, Japan) using the induction melting method. The chemical composition of the HAA powder was verified with a Varian Liberty 100 inductively coupled plasma-optical emission spectrometer (ICP-OES, Agilent Technologies, Santa Clara, CA, USA). Microstructure analysis was performed with a Philips X'Pert Pro X-ray diffractometer (XRD, Amsterdam, The Netherlands) and a JEOL-JSM6320F scanning electron microscope (SEM, Tokyo, Japan) with energy dispersive spectroscopy (EDS). A Suzuki-Shokan multi-channel pressure-concentration-temperature system (PCT, Tokyo, Japan) was used to measure the gaseous phase hydrogen storage (H-storage) characteristics. PCT measurements at 30 and 45 °C were performed after activation. A negative electrode sample was made by compacting the HAA powder onto an expanded nickel substrate through a roll mill without the use of a binder. The half-cell experiment, which employed a pre-activated sintered $Ni(OH)_2$ counter electrode and 30% KOH as the electrolyte, was performed using a CTE MCL2 Mini cell testing system (Chen Tech Electric Mfg. Co., Ltd., New Taipei, Taiwan). A Solartron 1250 Frequency Response Analyzer (Solartron Analytical, Leicester, UK) with a sine wave amplitude of 10 mV and a frequency range of 0.5 mHz–10 kHz was used for the alternative current (AC) impedance measurements. A Digital Measurement Systems Model 880 vibrating sample magnetometer (MicroSense, Lowell, MA, USA) was used to measure the magnetic susceptibility of the surfaces of the activated alloy powder (activation was performed by immersing the powder in 30 wt % KOH solution at 100 °C for 4 h).

3. Results and Discussion

Five superlattice HAAs (Fe1–Fe5) with a general composition of $Mm_{0.83}Mg_{0.17}Ni_{2.94-x}Al_{0.17}Co_{0.2}Fe_x$ (x = 0, 0.05, 0.1, 0.15, 0.2) were prepared for this study. Design compositions and ICP results in at% are listed in Table 1. The B/A ratio was set to 3.31, which is the same as in previous matrices for Mn [8] and Co substitutions [9], and the stoichiometry for the main Ce_2Ni_7 phase was independent of the overall composition [10]. The base alloy (Fe1) was chosen from a previous matrix of Co-substituted superlattice HAAs (C3) due to its superior low-temperature performance [9]. ICP results show that the composition of each alloy is very close to its designed value (Table 1).

Table 1. Designed compositions (in **bold**) and inductively coupled plasma (ICP) results in at%. Mm stands for misch metal (mixture of rare earth elements).

Alloy	Source	Mm	Mg	Ni	Al	Co	Fe	B/A
Fe1	**Design**	**19.3**	**3.9**	**68.2**	**3.9**	**4.6**	**0.0**	**3.31**
	ICP	19.2	4.0	68.0	4.0	4.7	0.1	3.32
Fe2	**Design**	**19.3**	**3.9**	**67.1**	**3.9**	**4.6**	**1.2**	**3.31**
	ICP	19.1	3.9	67.0	4.0	4.8	1.2	3.35
Fe3	**Design**	**19.3**	**3.9**	**65.9**	**3.9**	**4.6**	**2.3**	**3.31**
	ICP	19.1	4.0	65.8	4.0	4.7	2.4	3.33
Fe4	**Design**	**19.3**	**3.9**	**64.7**	**3.9**	**4.6**	**3.5**	**3.31**
	ICP	19.2	4.0	64.6	4.0	4.7	3.6	3.32
Fe5	**Design**	**19.3**	**3.9**	**63.6**	**3.9**	**4.6**	**4.6**	**3.31**
	ICP	19.1	4.0	63.4	4.0	4.7	4.7	3.31

3.1. X-Ray Diffraction Analysis

The powder XRD patterns of the five alloys in this study are shown in Figure 1. Peaks from the Ce_2Ni_7, $NdNi_3$, and $CaCu_5$ phases can easily be identified. The lattice parameters of the main phase (Ce_2Ni_7) and phase abundances of all three phases were calculated using the Rietveld refinement method with the Jade 9 software (Materials Data Inc. (MDI), Livermore, CA, USA), and the results are summarized in Table 2.
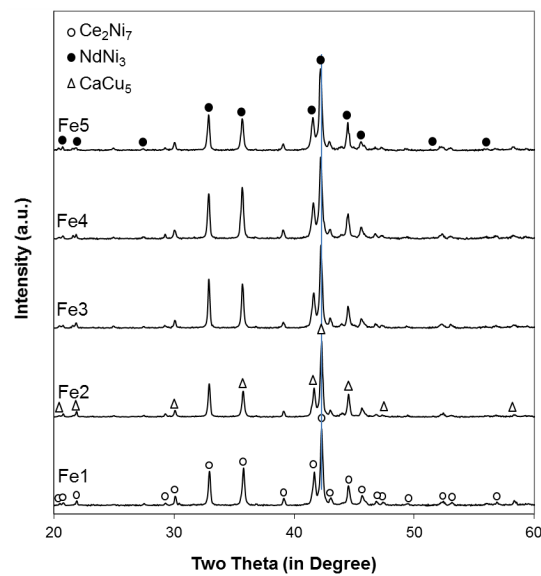

Figure 1. X-ray diffraction (XRD) patterns using a Cu–Kα radiation source for alloys Fe1–Fe5. The vertical line shows the shift in the main peak to lower angles (the unit cell becomes larger) with increasing Fe content.

Table 2. Lattice constants *a* and *c*, *c/a* ratio, unit cell volume, and crystallite size of the main Ce$_2$Ni$_7$ phase from a full-pattern fitting, and phase abundances calculated from XRD analysis of alloys Fe1–Fe5. Error ranges are indicated in parentheses after the lattice parameters. R: rhombohedral; and H: hexagonal.

Alloy	Fe1	Fe2	Fe3	Fe4	Fe5
Ce$_2$Ni$_7$ *a* (Å)	5.0198(3)	5.0228(4)	5.0282(5)	5.0306(4)	5.0321(3)
Ce$_2$Ni$_7$ *c* (Å)	24.3951(8)	24.4085(9)	24.4166(7)	24.4310(8)	24.4340(12)
Ce$_2$Ni$_7$ *c/a* ratio	4.860	4.860	4.856	4.856	4.856
Ce$_2$Ni$_7$ unit cell volume (Å^3)	532.36	533.29	534.61	535.44	535.83
Ce$_2$Ni$_7$ crystallite size (Å)	>1000	>1000	880	>1000	844
Ce$_2$Ni$_7$ (H) abundance (wt %)	58.0	62.3	66.4	66.6	68.0
NdNi$_3$ *a* (Å)	5.0265(3)	5.0363(4)	4.9782(5)	5.0399(5)	4.9539(3)
NdNi$_3$ *c* (Å)	24.4471(11)	24.4575(9)	24.7684(7)	24.7587(8)	23.9907(10)
NdNi$_3$ (R) abundance (wt %)	20.1	17.5	13.7	10.2	1.5
CaCu$_5$ *a* (Å)	5.0203(4)	5.0263(5)	5.0293(4)	5.0209(3)	5.0322(6)
CaCu$_5$ *c* (Å)	4.0693(3)	4.0692(4)	4.0706(6)	4.0729(5)	4.0716(6)
CaCu$_5$ (H) abundance (wt %)	21.9	20.2	19.8	23.2	30.4

As seen in Figure 2, both lattice parameters *a* and *c* of the main Ce$_2$Ni$_7$ phase increase with increasing Fe content (larger size compared to that of Ni), resulting in the unit cell expansions and, consequently, a shift in the main XRD peak (around 42.2°) to lower angles (larger interplanar distance), as indicated by the vertical line in Figure 1. Moreover, the roughly unchanged *c/a* ratios shown in Table 2 suggest that the Ce$_2$Ni$_7$ unit cell expansion is isotropic, which differs from the faster growth in the a-direction reported in the Mn-substitution study [8]. Changes in the Ce$_2$Ni$_7$ unit cell volume with Mn, Fe, and Co substitutions are compared in Figure 3. While the slopes of graphs representing increase versus substitution amount for the Mn and Fe substitutions are similar, no change is observed for the Co substitution due to the similarity in atomic radii between Co and the replaced Ni. Additionally, no particular trend in Ce$_2$Ni$_7$ crystallite size (determined by the full width at half-maximum of the (109) peak) with increasing Fe content can be established, which differs from the Mn (decreasing) [8] and Co substitutions (increasing) [9].
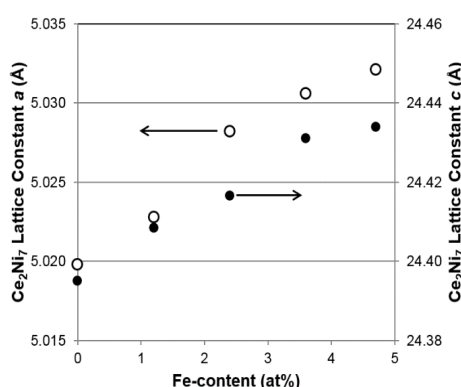
Figure 2. Changes in the Ce$_2$Ni$_7$ phase lattice constants *a* and *c* with the designed change in Fe content.

Phase abundances of the three constituent phases from the Mn, Fe, and Co substitution studies are plotted in Figure 4. It should be noted that phases with the same composition are merged into one category. For example, calculations for the A$_2$B$_7$ phase abundance include both the hexagonal (Ce$_2$Ni$_7$) and rhombohedral (Pr$_2$Ni$_7$) phase structures. Compared to the large fluctuations in A$_2$B$_7$ phase abundance for the Mn and Co substitutions, the Fe substitution increases the amount of the main A$_2$B$_7$ phase (Figure 4a). The electrochemical performance of the A$_2$B$_7$ phase was believed to be superior to that of the AB$_3$ phase [45]. However, while additives, including Ce, Nd, Pr, Sm, Zr, Ti, Si,

and Cr, decreased the A_2B_7 phase abundance, only Fe and Cu were found to increase the abundance of this phase [46]. It is clear from the comparison shown in Figure 4b that Mn promotes and Fe decreases the AB_3 phase formation. Meanwhile, the effect of Co in this case is not obvious. Trends in AB_5 phase abundance are similar for the increases in all three substitutions, except for the alloy with the least amount of Mn in the Mn-series, and exhibit the behavior of first decreasing and then increasing. Among the three substitutions, the average amount of the AB_5 phase abundance increases in the following trend: Mn < Co < Fe.
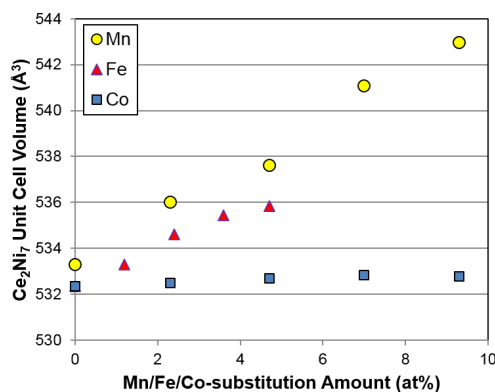

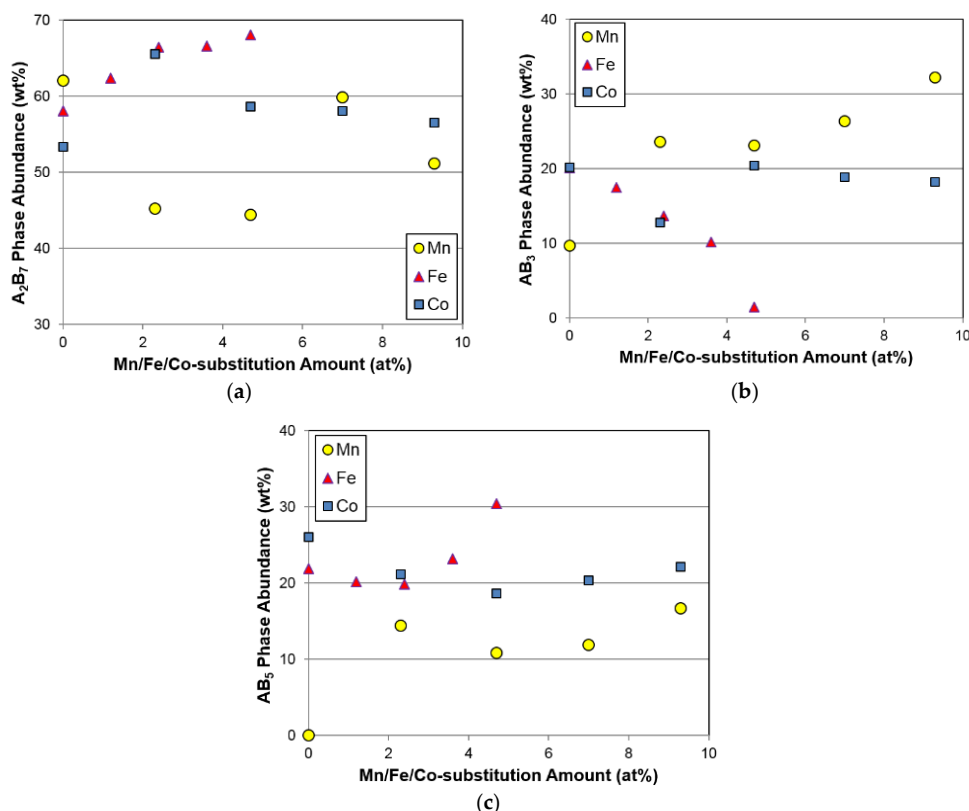**Figure 3.** Comparison of Ce_2Ni_7 unit cell volumes with different substitutions.

Figure 4. Changes in the (**a**) A_2B_7; (**b**) AB_3; and (**c**) AB_5 phase abundances with increasingdf substitution amounts.

3.2. Scanning Electron Microscope/Energy Dispersive Spectroscopy Analysis

SEM analysis was performed on the polished powder sample surface, and the backscattered electron (BSE) micrographs of the five alloys are shown in Figure 5. In general, the color intensity of each image is very uniform, with some occasional brighter spots and/or areas with slightly darker

contrasts. The chemical composition of the numbered areas in each BSE micrograph were studied by EDS, and the results are summarized in Table 3. Brighter spots (Figure 5a-2,b-2) are an excess of rare earth metals, and the darker areas are either the AB_5 (Figure 5b-3,d-2) or $LaMgNi_4$ (Figure 5c-2,e-2) phase. The AB_3 and A_2B_7 phases cannot be separated due to their similarity in composition. The B/A ratios in the main AB_3/A_2B_7 phase of alloys Fe1–Fe5 are in the range of 3.31–3.41, which is between the B/A ratios of AB_3 (3.0) and A_2B_7 (3.5) and closer to the B/A ratio of A_2B_7 (3.5). This finding is in agreement of the XRD results, where the A_2B_7 phase abundance was found to be higher than the AB_3 phase abundance. Similar to the cases of Mn and Co substitutions, Fe does not form any separated secondary phase and dissolves completely in the main AB_3/A_2B_7 phase. Therefore, changes in the lattice constant of the main phase, as revealed by XRD, were the result of Fe incorporation. EDS analysis also shows that the $LaMgNi_4$ phase is deficient in Al, Co, and Fe, while the AB_5 phase is rich in Al, Co, and Fe.
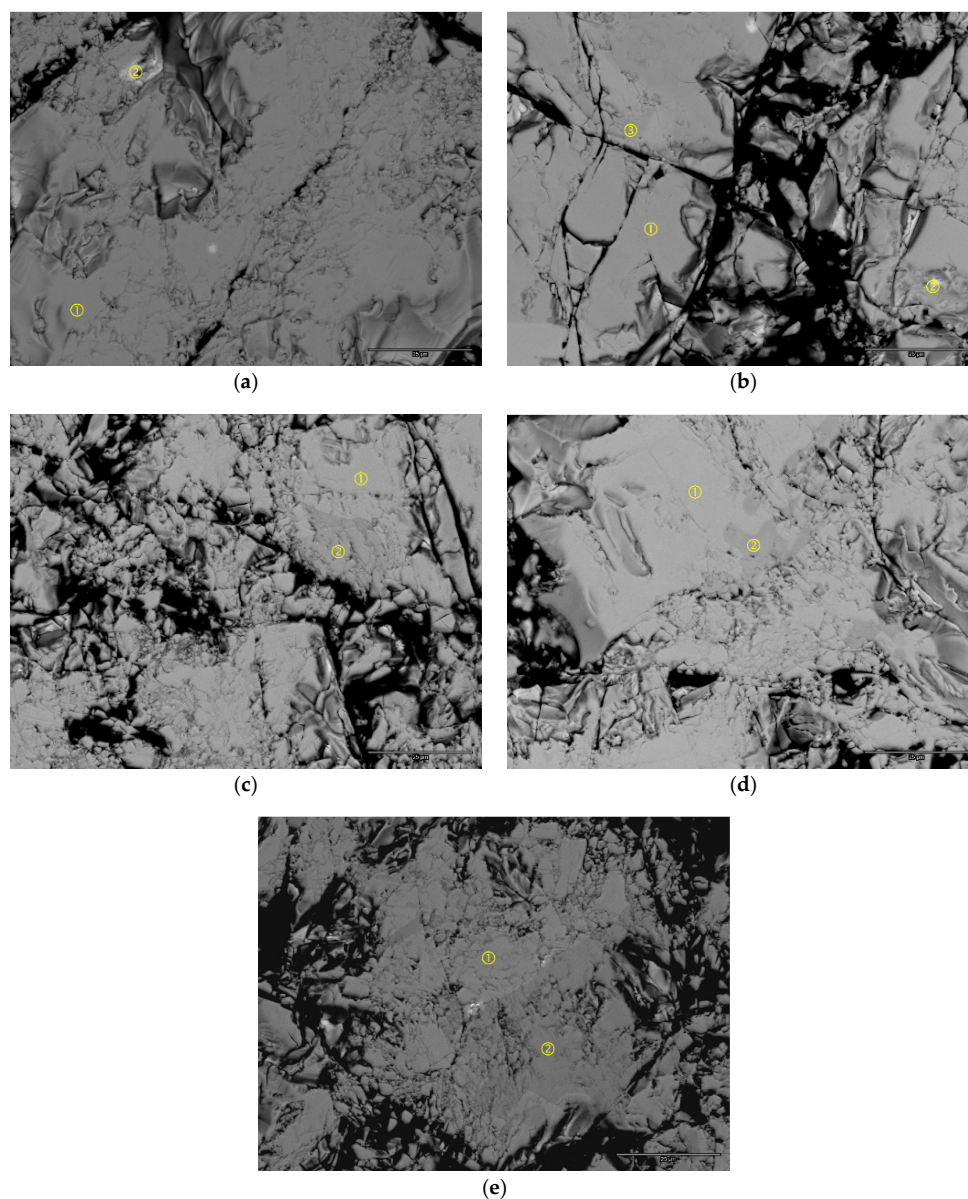

Figure 5. Scanning electron microscope-backscattered electron (SEM-BSE) micrographs from alloys (**a**) Fe1; (**b**) Fe2; (**c**) Fe3; (**d**) Fe4; and (**e**) Fe5. The bar on the lower right corner represents 25 microns. The composition of the numbered areas was analyzed by energy dispersive spectroscopy (EDS), and results are available in Table 3.

Table 3. Summary of EDS results. All compositions are in at%. The composition of the main phase is in **bold**.

Sample	Location	La	Pr	Nd	Mg	Ni	Al	Co	Fe	Mg/A	B/A	Phase
Fe1	**Figure 5a-1**	**3.9**	**8.0**	**8.0**	**3.0**	**68.6**	**3.8**	**4.7**	**0.0**	**0.13**	**3.37**	**AB_3/A_2B_7**
	Figure 5a-2	41.6	27.3	26.7	0.0	3.9	0.5	0.0	0.0	0.00	0.05	Rare Earth
Fe2	**Figure 5b-1**	**4.0**	**7.9**	**7.9**	**3.0**	**66.2**	**4.7**	**5.2**	**1.1**	**0.13**	**3.39**	**AB_3/A_2B_7**
	Figure 5b-2	43.4	22.7	21.1	0.0	11.6	0.8	0.4	0.0	0.00	0.15	Rare Earth
	Figure 5b-3	2.8	7.2	7.8	0.6	69.0	5.2	6.0	1.4	0.03	4.43	AB_5
Fe3	**Figure 5c-1**	**4.2**	**8.0**	**8.0**	**3.0**	**65.5**	**4.3**	**4.8**	**2.2**	**0.13**	**3.31**	**AB_3/A_2B_7**
	Figure 5c-2	3.1	8.1	8.3	14.3	61.7	0.8	2.7	1.0	0.42	1.96	$LaMgNi_4$
Fe4	**Figure 5d-1**	**3.8**	**7.8**	**7.9**	**3.3**	**64.7**	**4.8**	**4.4**	**3.3**	**0.14**	**3.39**	**AB_3/A_2B_7**
	Figure 5d-2	3.2	6.8	6.9	0.4	64.3	8.3	5.3	4.8	0.02	4.78	AB_5
Fe5	**Figure 5e-1**	**4.4**	**8.0**	**7.9**	**2.4**	**62.8**	**4.4**	**5.1**	**5.0**	**0.11**	**3.41**	**AB_3/A_2B_7**
	Figure 5e-2	3.0	8.0	7.9	15.0	60.7	0.8	2.8	1.8	0.44	1.95	$LaMgNi_4$

3.3. Gaseous Phase Hydrogen Storage

The gaseous phase H-storage characteristics of the alloys were studied using PCT measurements performed at 30 and 45 °C. The PCT isotherms are plotted in Figure 6. In general, the changes in shape and position of the isotherms from the Fe-incorporated alloys are small. The isotherms are similar to those from the Co-incorporated alloys [9], but different from the Mn-incorporated alloys [8].
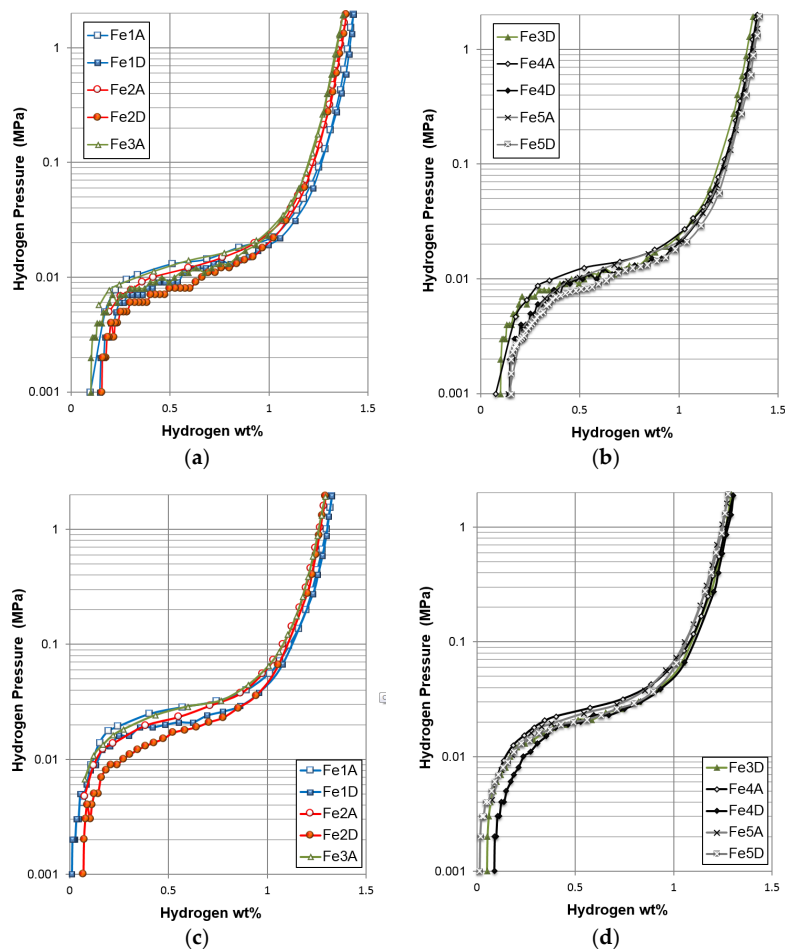

Figure 6. Pressure-concentration-temperature (PCT) isotherms measured at (**a**,**b**) 30 and (**c**,**d**) 45 °C for alloys Fe1–Fe5. A and D denote absorption and desorption, respectively. The plateau region has been expanded in the inset.

Several gaseous phase parameters obtained from the PCT measurements are listed in Table 4. Maximum H-storage at 30 °C decreases marginally and then increases slightly with increasing Fe content. Furthermore, changes in maximum and reversible H-storage with the Fe substitution are small, which again reflects similar results to Co substitution, but is unlike the results obtained with Mn substitution (Figure 7a,b). Unexpectedly, increases in unit cell volume (Figure 3) and abundance (Figure 4a) of the main Ce_2Ni_7 phase with increasing Fe content do not increase the gaseous phase H-storage, suggesting that a synergetic effect between the main and secondary phases may dominate the H-storage performance in the Fe-substituted alloys. However, the exact mechanism is not clear at the present time.

Table 4. Summary of gaseous phase hydrogen storage (H-storage) properties. Error ranges are indicated in parentheses after the quantity. PCT: pressure-concentration-temperature; and SF: slope factor.

H-storage Properties	Alloy				
	Fe1	**Fe2**	**Fe3**	**Fe4**	**Fe5**
Maximum Capacity @ 30 °C (wt %)	1.43	1.39	0.37	0.39	1.41
Reversible Capacity @ 30 °C (wt %)	1.28	1.23	0.27	1.25	1.25
Desorption Pressure@ 0.75%, 30 °C (MPa)	0.0138	0.0116	0.0130	0.0123	0.0128
Desorption Pressure @ 0.75%, 45 °C (MPa)	0.0254	0.0222	0.266	0.261	0.0273
PCT Hysteresis @ 0.75%, 30 °C	0.14	0.23	0.21	0.21	0.14
PCT Hysteresis @ 0.75%, 45 °C	0.24	0.35	0.19	0.22	0.12
PCT SF @ 30 °C	0.83	0.81	0.83	0.79	0.77
PCT SF @ 45 °C	0.84	0.82	0.85	0.82	0.82
$-\Delta H$ (kJ·mol^{-1})	33 (2)	35 (2)	38 (2)	40 (2)	41 (2)
$-\Delta S$ (J·mol^{-1}·K^{-1})	91 (3)	97 (3)	109 (3)	115 (3)	116 (4)
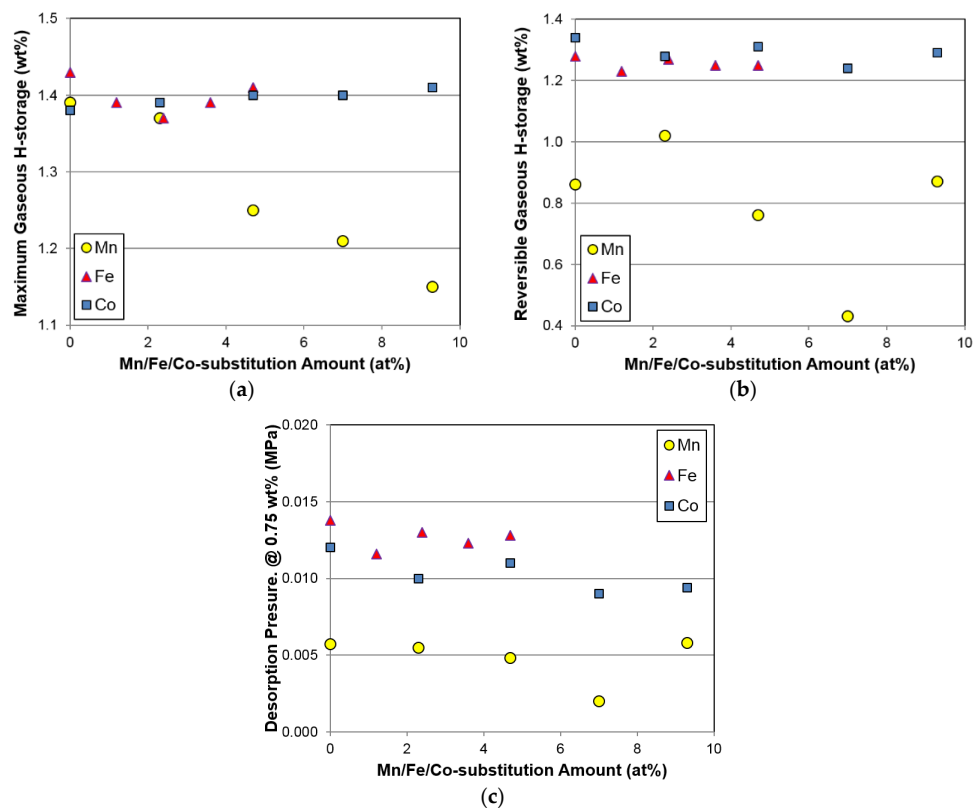
Figure 7. Changes in the (**a**) maximum and (**b**) reversible H-storage capacities; and (**c**) desorption plateau pressure at 0.75 wt % H-storage obtained from the 30 °C PCT isotherms with increasing substitution amount.

Due to the multi-phase nature of the superlattice HAA, the plateau region of the PCT isotherm is not well defined. Therefore, the desorption pressure at 0.75 wt % H-storage is used instead of the plateau pressure in this study. Changes in desorption pressure at 0.75 wt % H-storage for the Fe-substituted alloys were very small, which is similar to what occurs with Co and Mn substitutions (Figure 7c). Composition modifications with Al [11] and La [12] are more effective in changing the equilibrium pressure.
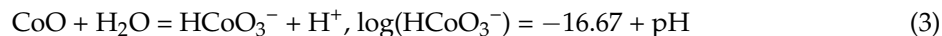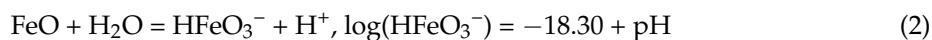
PCT hysteresis is defined as ln(absorption pressure at 0.75 wt % H-storage/desorption pressure at 0.75 wt %). PCT hysteresis is an indication of the elastic deformation energy needed to overcome the lattice expansion at the metal (α)-hydride (β) interface and has been used to predict the pulverization rate during hydride/dehydride cycling [47]. Both PCT hystereses measured at 30 and 45 °C increase and then decrease with increasing Fe content. In addition, Fe-substituted alloys show smaller PCT hysteresis compared to the Mn- and Co-substituted alloys.

Slope factor (SF), defined as the ratio of the H-storage capacity between 0.005 and 0.2 MPa and the reversible H-storage, is related to the degree of homogeneity in the alloy. More specifically, a higher SF value corresponds to a higher uniformity and lesser degree of disorder in the alloy. For the Fe-substituted alloys, SF is independent of Fe content, and the SFs measured at 30 °C are lower than those at 45 °C. Addition of Fe does not alter the alloy homogeneity, which is similar to the case of Co incorporation [9], but different from Mn incorporation, where a reduction in homogeneity was observed [8].

Two thermodynamic parameters, the changes in enthalpy (ΔH) and entropy (ΔS), were estimated using the Van't Hoff equation and the results are listed in Table 4. With increasing Fe content, both ΔH and ΔS become more negative, indicating the formation of a more stable (involving stronger metal–hydrogen (M–H) bonding) and ordered hydride. Compared to the results obtained previously [8,9], the influences on both ΔH and ΔS from Fe are stronger than those from Co and Mn. If we only focus on the Fe-substituted alloys, we may reach the conclusion that with increasing Fe content, the unit cell volume of the main Ce_2Ni_7 phase increases, resulting in a more stable hydride. However, compared to the Fe-substituted alloys, the Mn-substituted alloys have larger Ce_2Ni_7 unit cells, but higher ΔHs. Therefore, the correlation between the structural properties and gaseous phase H-storage characteristics may be too convoluted to establish due to the complex and multi-phase nature of the superlattice alloys.

3.4. Electrochemical Analysis

The open-to-atmosphere half-cell configuration was used to measure the discharge capacities of the five alloys in this study. The dry-compacted electrode was charged with a current density of 100 mA·g^{-1} for 5 h, and it was then discharged initially with the same current density and followed by two pulls at 24 and 8 mA·g^{-1}. These three discharge capacities were added, and the sum considered as the full discharge capacity measured at 8 mA·g^{-1}. In order to examine the activation behaviors, full discharge capacities and HRDs (the ratio of the high-rate discharge capacity to the full discharge capacity) from the first 13 cycles for the five alloys in this study are plotted in Figure 8. Compared to the capacity and HRD curves from the Mn- and Co-substituted alloys, Fe does not facilitate the formation process in the same manner as Mn and Co, which is possibly due to the relatively low solubility of Fe in alkaline solutions, as shown by the following comparison [48]:

$$MnO + H_2O = HMnO_3^- + H^+, \log(HMnO_3^-) = -16.57 + pH \tag{1}$$

$$FeO + H_2O = HFeO_3^- + H^+, \log(HFeO_3^-) = -18.30 + pH \tag{2}$$

$$CoO + H_2O = HCoO_3^- + H^+, \log(HCoO_3^-) = -16.67 + pH \tag{3}$$

Achievable concentrations of soluble Mn and Co ions are higher than for soluble Fe ion, indicating that Mn and Co are more soluble compared to Fe and therefore contribute positively to the activation

performance. Both the full and high-rate discharge capacities, together with HRD, are listed in Table 5. A lower amount of Fe ($\leq$2.3 at%) does not affect the capacity or HRD significantly, but a larger amount of Fe deteriorates both the capacities and HRD. Moreover, the reduction in discharge capacity does not correlate well with the relatively unchanged gaseous phase H-storage values (Figure 7a,b).
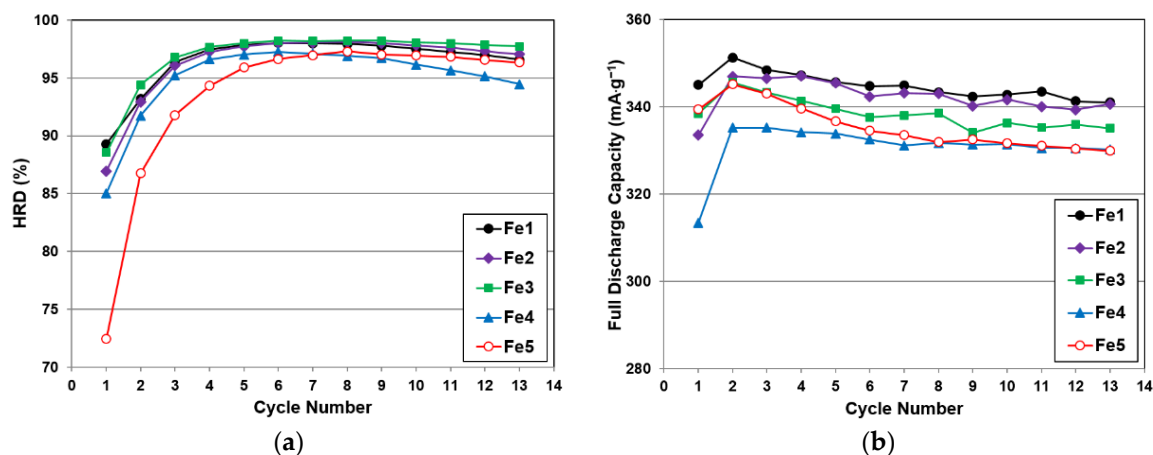
Figure 8. Activation characteristics over the first 13 cycles demonstrating (**a**) full discharge capacity with the lowest discharge current (8 mA·g^{-1}); and (**b**) high-rate dischargeability (HRD) for alloys Fe1–Fe5.

Table 5. Summary of electrochemical properties: capacity, rate, bulk diffusion coefficient (*D*), and surface exchange current (I_o). RT stands for room temperature.

| Alloy	2nd Cycle High-Rate Capacity (mAh·g^{-1})	2nd Cycle Full Capacity (mAh·g^{-1})	HRD (%)	D @ RT (10^{-10} cm^2·s^{-1})	I_o @ RT (mA·g^{-1})
Fe1	327	351	0.93	5.2	37.5
Fe2	322	347	0.93	4.7	37.2
Fe3	326	346	0.94	3.5	25.7
Fe4	308	335	0.92	3.4	23.6
Fe5	299	345	0.87	2.7	20.5

Changes in full capacity, high-rate capacity, and HRD with different substitution elements are compared in Figure 9a–c, respectively. While Co substitution slightly improves both the full and high-rate capacities, Mn and Fe substitutions (>2.3 at%) decrease the capacities and HRD.

In order to trace the source of the degradations in electrochemical capacities and HRD, both the bulk hydrogen diffusion constant (*D*) and surface exchange current (I_o) were measured electrochemically (a detailed methodology were reported in our earlier publications [9,49]), and the results are summarized in Table 5. Since *D* decreases monotonically from the initial measurements, while I_o decreases when the Fe content is greater than 1.2 at%, both bulk hydrogen diffusion and surface catalytic ability deteriorate with Fe incorporation. The decrease in *D* may be due to a decrease in abundance of the AB$_3$ secondary phase, which decreases the synergetic effects and is an indispensable element in electrochemical H-storage in a multi-phase HAA system [50,51]. Similar to the case in the Laves phase-related bcc solid solution HAA system, where C14 (with stronger M–H bonding) serves as the catalytic phase for the bcc storage phase (with weaker M–H bonding) [51], the AB$_3$ phase can also serve as the catalytic phase that contributes to the synergetic effects despite the fact that it has stronger M–H bonding (judging from its lower B/A ratio compared to the main A$_2$B$_7$ phase). By reducing the AB$_3$ phase abundance through Fe incorporation, the synergetic effects are lowered and, consequently, the hydrogen diffusion in the alloy bulk is impeded. Furthermore, the observed decrease in I_o may be caused by the differences in alloy surface created by addition of Fe, which will be further investigated in the next section. From the observations of *D* and I_o, it can be concluded that both poor bulk diffusion and surface reaction properties are responsible for the decrease in HRD

seen with Fe incorporation. Changes in D and I_o with different substitution elements are compared in Figure 10, and both Mn and Fe result in deterioration, but Co improves the bulk hydrogen diffusion and surface electrochemical reaction.
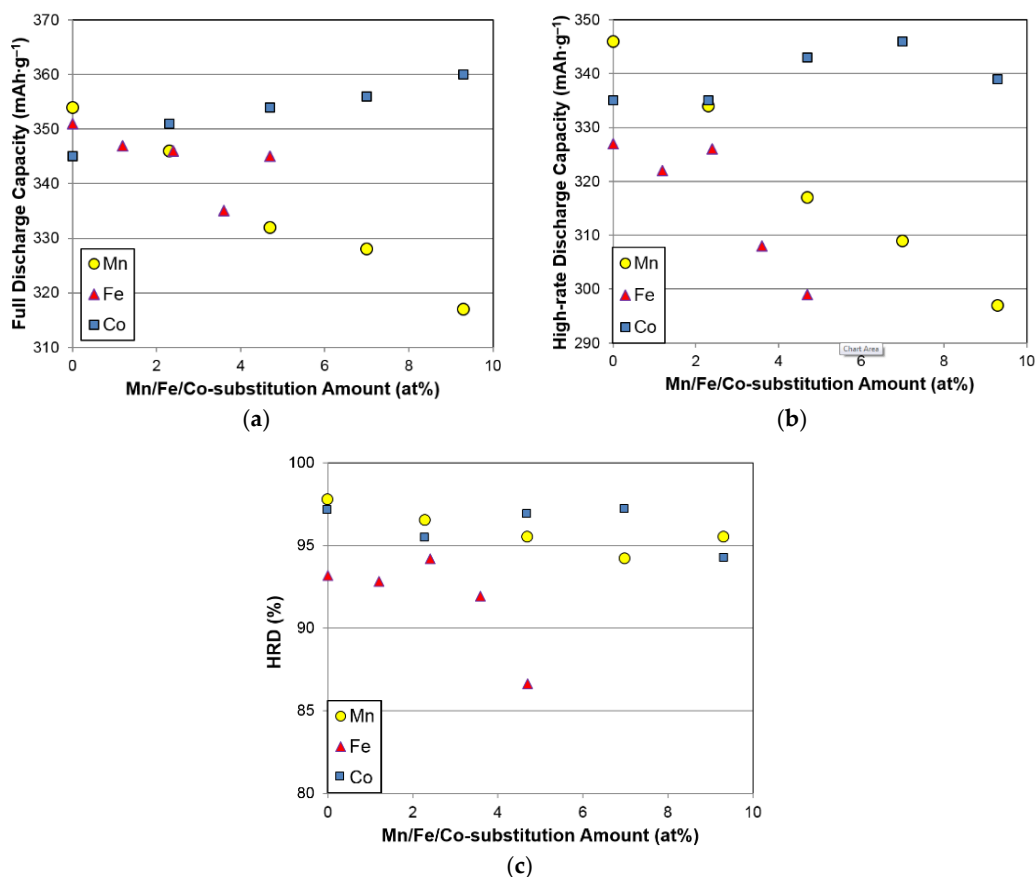
Figure 9. Changes in (**a**) full and (**b**) high-rate (100 mA·g^{-1}) capacities; and (**c**) their ratios (HRD) with increasing substitution amounts.
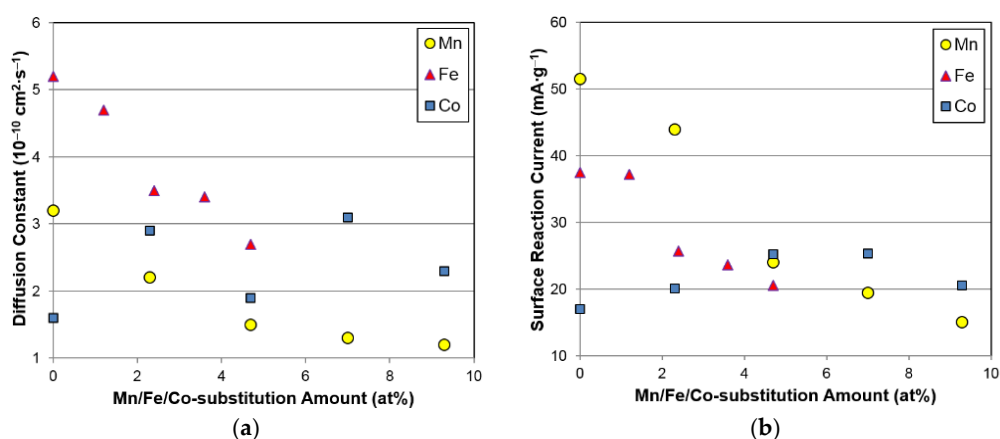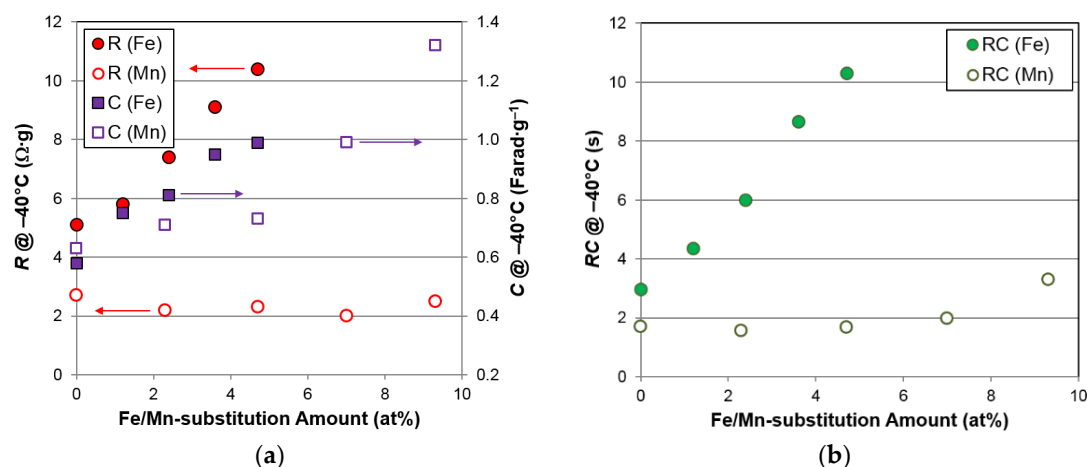

Figure 10.　Changes in (**a**) bulk diffusion constant (D) and (**b**) surface reaction current (I_o) with increasing substitution amounts.

Overcoming low-temperature performance (especially at −40 °C) in Ni/MH batteries has always been a very challenging task [52]. We have consistently chosen the AC impedance measurement as the main tool for investigating the −40 °C electrochemical reaction [53,54]. Details regarding the

experimental setup can be found in our earlier publications [55,56]. Surface charge-transfer resistances (*R*) and surface double-layer capacitances (*C*) obtained from the Cole–Cole plots measured at both room temperature and $-40\,°$C are summarized in Table 6. In general, R_s and C_s measured at room temperature and $-40\,°$C increase with increasing Fe content. An increase in the reactive surface area (proportional to *C*) with Fe incorporation was also reported for the AB$_2$ [21] and AB$_5$ HAAs [29]. However, the contributions of Fe to *R* vary for the AB$_2$ [21] and AB$_5$ HAAs; *R* decreases in AB$_2$ [21], but increases in AB$_5$ [34]. The *RC* product has been previously used to characterize the surface catalytic ability [29,34]. With increasing Fe content, the *RC* product increases in the current study and for the AB$_5$ HAA [34], but it decreases with the AB$_2$ HAA [29], which suggests that Fe incorporation impedes the surface electrochemical reaction of A$_2$B$_7$ and AB$_5$, but facilitates that of AB$_2$. *R*, *C*, and *RC* measured at $-40\,°$C for the Fe- and Mn-substituted superlattice alloys are compared in Figure 11. Although Fe promotes an increase in the surface area more effectively than Mn, the resistances of Fe-containing alloys are much higher than those of the Mn-containing alloys, due to the loss of surface catalytic ability with Fe incorporation, as indicated by the *RC* plot in Figure 11c.

Table 6. Summary of alternative current (AC) impedance and magnetic susceptibility measurement results. *R*, *C*, M_S, and $H_{1/2}$ represent the charge transfer resistance, double-layer capacitance, saturated magnetic susceptibility, and magnetic field at half of M_S, respectively.

| Alloy	*R* @ RT ($\Omega \cdot$g)	*C* @ RT (Farad·g^{-1})	*RC* @ RT (s)	*R* @ $-40\,°$C ($\Omega \cdot$g)	*C* @ $-40\,°$C (Farad·g^{-1})	*RC* @ $-40\,°$C (s)	M_S (memu·g^{-1})	$H_{1/2}$ (kOe)
Fe1	0.11	0.30	0.03	5.1	0.58	2.9	1016	0.128
Fe2	0.10	0.42	0.04	5.8	0.75	4.3	835	0.109
Fe3	0.15	0.37	0.06	7.4	0.81	6.0	718	0.106
Fe4	0.13	0.71	0.09	9.1	0.95	8.7	481	0.091
Fe5	0.13	0.82	0.11	10.4	0.99	10.3	341	0.060

(a)   **(b)**

Figure 11. Changes in (**a**) charge transfer resistance (*R*) and double-layer capacitance (*C*) calculated from the AC impedance measured at $-40\,°$C; and (**b**) their product (*RC*) with increasing substitution amounts. A larger *RC* product corresponds to a slower surface electrochemical reaction and a less catalytic surface.

3.5. Magnetic Properties

The source of degradation in the surface catalytic ability for the Fe-containing superlattice HAAs was further investigated using magnetic susceptibility measurements. Due to the large difference (more than seven orders of magnitude) in the saturated magnetic susceptibilities (M_S) of elemental Ni and Ni in HAA, M_S has been used to estimate the total volume of the metallic Ni clusters imbedded in the surface oxide formed during activation [57]. This measurement has been successfully correlated to HRD of HAA [58]. Moreover, the strength of the applied magnetic field corresponding to half of the M_S

value ($H_{1/2}$) is inversely proportional to the magnetic domain size and used as an indicator of the size of metallic clusters in the surface oxide [59]. Both the M_S and $H_{1/2}$ values obtained from the five alloys in this study are listed in Table 6 and plotted with the data from Mn- and Co-substitution studies [8,9] in Figure 12. With increasing Fe content, both M_S and $H_{1/2}$ decrease, suggesting that Fe incorporation decreases the total volume and surface area of catalytic Ni clusters, judging from the increase in cluster size indicated by the reduction in $H_{1/2}$. The reduction in the amount of catalytic Ni clusters in the surface oxide for the Fe-containing alloys explains the observed decreases in surface catalytic ability, as indicated by the increase in RC in Figure 11c and the surface reaction current (Figure 10b), causing the deterioration in HRD (Figure 9). In addition, the M_Ss of the Mn- and Co-containing alloys are slightly lower than those seen in the base alloy (free of Mn and Co), which suggests that the amount of Ni in the alloy composition correlates closely to the amount of metallic Ni in the surface oxide after activation. Partial replacement of Mn, Fe, and Co for Ni may benefit several electrochemical properties, but certainly deteriorate the high-rate and low-temperature performances due to the reduction in amount of surface catalytic Ni clusters. Interestingly, it was also observed that both $H_{1/2}$ and the AB_3 phase abundance demonstrate similar trends (Figures 4b and 12), and such correlations will be verified in the future.
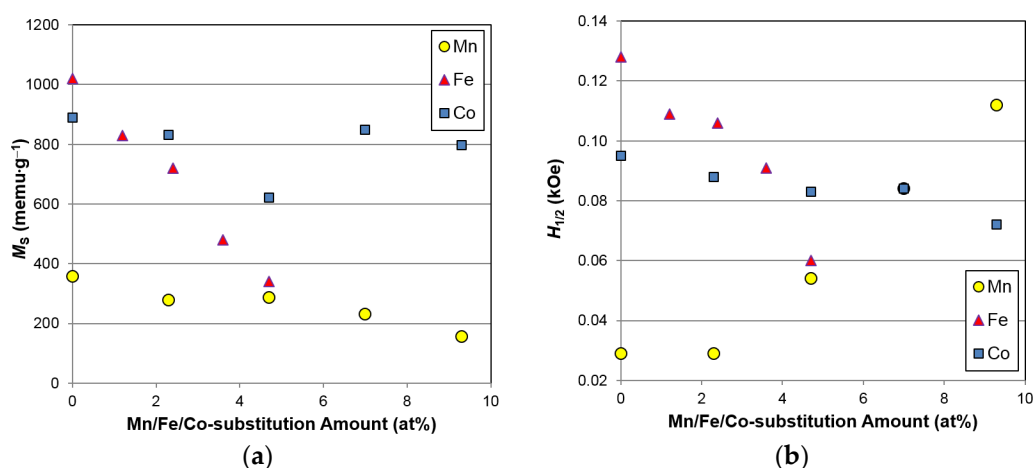
Figure 12. Changes in (**a**) saturated magnetic susceptibility (M_S); and (**b**) strength of the applied magnetic field corresponding to half of M_S ($H_{1/2}$) with increasing substitution amounts.

4. Conclusions

The effects of partial replacement of Ni with Fe in the misch metal-based superlattice HAA were studied and compared with those Mn and Co substitutions. An increase in abundance of the favorable Ce_2Ni_7 phase with Fe incorporation does not significantly affect the H-storage capacity, but the electrochemical properties degraded. Partial replacement of Ni with Fe results in a reduction in total volume of surface metallic Ni inclusions and, consequently, lowers the surface electrochemical reactivity. Even with an increase in the reactive surface area, the Fe-containing alloys exhibit higher surface resistivity at both room temperature and −40 °C, due to severely deteriorated surface catalytic ability. Among various studied substitutions, Co is a better substituting element with regards to general electrochemical performance. However, the Fe-substituting-Ni studied in this work exhibits an increase in the beneficial Ce_2Ni_7 phase abundance and decreases the relatively unfavorable $NdNi_3$ phase among all the AB_3-type phases. Therefore, although Fe incorporation deteriorates most electrochemical properties, further surface treatment may be needed to improve the surface catalytic ability and reveal the positive contribution that Fe structurally provides. Moreover, alternative substitutions targeted to improve the low-temperature performance in Ni/MH battery, such as Mo and Cu, will also be studied in the near future.

Author Contributions: Kwo-Hsiung Young designed the experiments and analyzed the results. Taihei Ouchi prepared the alloy samples and performed the PCT and XRD analyses. Jean Nei prepared the electrode samples and conducted the magnetic measurements. Shigekazu Yasuoka designed and obtained the test samples.

Conflicts of Interest: The authors declare no conflict of interest.

Abbreviations

HAA	Hydrogen absorbing alloy
Ni/MH	Nickel/metal hydride
bcc	Body-centered-cubic
HRD	High-rate dischargeability
ICP-OES	Inductively coupled plasma-optical emission spectrometer
XRD	X-ray diffractometer
SEM	Scanning electron microscope
EDS	Energy dispersive spectroscopy
PCT	Pressure-concentration-temperature
AC	Alternative current
H-storage	Hydrogen storage
BSE	Backscattered electron
α	Metal phase or alloy matrix
β	Hydride phase
SF	Slope factor
M–H	Metal–hydrogen
ΔH	Change in enthalpy or heat of hydride formation
ΔS	Change in entropy
D	Bulk hydrogen diffusion coefficient
I_o	Surface exchange current
R	Surface charge-transfer resistance
C	*S*urface double-layer capacitance
RT	Room temperature
M_S	Saturated magnetic susceptibility
$H_{1/2}$	Applied magnetic field strength corresponding to half of saturated magnetic susceptibility

References

1. Yasuoka, S.; Magari, Y.; Murata, T.; Tanaka, T.; Ishida, J.; Nakamura, H.; Nohma, T.; Kihara, M.; Baba, Y.; Teraoka, H. Development of high-capacity nickel-metal hydride batteries using superlattice hydrogen-absorbing alloys. *J. Power Sources* **2006**, *156*, 662–666. [CrossRef]

2. Teraoka, H. Development of Low Self-Discharge Nickel-Metal Hydride Battery. 2007. Available online: http://www.scribd.com/doc/9704685/Teraoka-Article-En (accessed on 9 April 2016).

3. Kai, T.; Ishida, J.; Yasuoka, S.; Takeno, K. The Effect of Nickel-Metal Hydride Battery's Characteristics with Structure of the Alloy. In Proceedings of the 54th Battery Symposium, Osaka, Japan, 7–9 October 2013; p. 210.

4. Takasaki, T.; Nishimura, K.; Saito, M.; Fukunaga, H.; Iwaki, T.; Sakai, T. Cobalt-free nickel-metal hydride battery for industrial applications. *J. Alloy. Compd.* **2013**, *580*, S378–S381. [CrossRef]

5. Crivello, J.C.; Zhang, J.; Latroche, M. Structural stability of AB_y phases in the (La,Mg)–Ni system obtained by density functional theory calculations. *J. Phys. Chem. C* **2011**, *115*, 25470–25478. [CrossRef]

6. Young, K.; Nei, J. The current status of hydrogen storage alloy development for electrochemical applications. *Materials* **2013**, *6*, 4574–4608. [CrossRef]

7. Verbovyts'kyi, Y.V.; Zavalii, I.Y. New metal-hydride electrode materials based on $R_{1-x}Mg_xNi_{3-4}$ alloys for chemical current sources. *Mater. Sci.* **2016**, *51*, 443–456. [CrossRef]

8. Young, K.; Wong, D.F.; Wang, L.; Nei, J.; Ouchi, T.; Yasuoka, S. Mn in misch-metal based superlattice metal hydride alloy—Part 1 Structural, hydrogen storage and electrochemical properties. *J. Power Sources* **2015**, *277*, 426–432. [CrossRef]

9. Wang, L.; Young, K.; Meng, T.; Ouchi, T.; Yasuoka, S. Partial substitution of cobalt for nickel in mixed rare earth metal based superlattice hydrogen absorbing alloy—Part 1 Structural, hydrogen storage and electrochemical properties. *J. Alloy. Compd.* **2016**, *660*, 407–415. [CrossRef]

10. Young, K.; Ouchi, T.; Huang, B. Effects of annealing and stoichiometry to (Nd, Mg)(Ni, Al)$_{3.5}$ metal hydride alloys. *J. Power Sources* **2012**, *215*, 152–159. [CrossRef]

11. Young, K.; Ouchi, T.; Wang, L.; Wong, D.F. The effected of Al substitution on the phase abundance, structure and electrochemical performance of La$_{0.7}$Mg$_{0.3}$Ni$_{2.8}$Co$_{0.5-x}$Al$_x$ (x = 0, 0.1, 0.2) alloys. *J. Power Sources* **2015**, *279*, 172–179. [CrossRef]

12. Yasuoka, S.; Ishida, J. Effects of cerium (Ce) on the hydrogen absorption-desorption characteristics of RE-Mg-Ni hydrogen absorbing alloy. Unpublished work. 2016.

13. Young, K.; Wong, D.F.; Wang, L.; Nei, J.; Ouchi, T.; Yasuoka, S. Mn in misch-metal based superlattice metal hydride alloy—Part 2 Ni/MH battery performance and failure mechanism. *J. Power Sources* **2015**, *277*, 433–442. [CrossRef]

14. Wang, L.; Young, K.; Meng, T.; English, N.; Yasuoka, S. Partial substitution of cobalt for nickel in mixed rare earth metal based superlattice hydrogen absorbing alloy—Part 2 Battery performance and failure mechanism. *J. Alloy. Compd.* **2016**, *664*, 417–427. [CrossRef]

15. Huang, T.; Wu, Z.; Huang, T.; Ni, J. Influence of V and Fe on the performance of TiMn$_2$ hydrogen storage alloy. *J. Funct. Mat. Devices* **2003**, *9*, 83–86.

16. Li, S.L.; Cheng, H.H.; Deng, X.X.; Chen, W.; Chen, D.M.; Yang, K. Investigation on hydrogen absorption/desorption properties of ZrMn$_{0.85-x}$Fe$_{1+x}$ alloys. *J. Alloy. Compd.* **2008**, *460*, 186–190. [CrossRef]

17. Jain, A.; Jain, R.K.; Agarwal, S.; Ganesan, V.; Lalla, N.P.; Phase, D.M.; Jain, I.P. Synthesis, characterization and hydrogenation of ZrFe$_{2-x}$Ni$_x$ (x = 0.2, 0.4, 0.6, 0.8) alloys. *Int. J. Hydrog. Energy* **2007**, *32*, 3965–3971. [CrossRef]

18. Song, M.Y.; Ahn, S.; Kwon, I.H.; Lee, R.; Rim, H. Development of AB$_2$-type Zr–Ti–Mn–V–Ni–Fe hydride electrodes for Ni–MH secondary batteries. *J. Alloy. Compd.* **2000**, *298*, 254–260. [CrossRef]

19. Song, M.Y.; Kwon, I.H.; Ahn, D.S.; Sohn, M.S. Improvement in the electrochemical properties of ZrMn$_2$ hydrides by substitution of elements. *Met. Mater. Int.* **2001**, *7*, 257–263. [CrossRef]

20. Young, K.; Fetcenko, M.A.; Koch, J.; Morii, K.; Shimizu, T. Studies of Sn, Co, Al, and Fe additives in C14/C15 Laves alloys for NiMH battery application by orthogonal arrays. *J. Alloy. Compd.* **2009**, *486*, 559–569. [CrossRef]

21. Young, K.; Ouchi, T.; Huang, B.; Reichman, B.; Fetcenko, M.A. The structure, hydrogen storage, and electrochemical properties of Fe-doped C14-predominating AB$_2$ metal hydride alloys. *Int. J. Hydrog. Energy* **2011**, *36*, 12296–12304. [CrossRef]

22. Young, K.; Ouchi, T.; Huang, B.; Ftecenko, M.A. Effects of B, Fe, Gd, Mg, and C on the structure, hydrogen storage, and electrochemical properties of vanadium-free AB$_2$ metal hydride alloy. *J. Alloy. Compd.* **2012**, *511*, 242–250. [CrossRef]

23. Ayari, M.; Paul-Boncour, V.; Lamloumi, J.; Percheron-Guégan, A. Magnetic properties of LaNi$_{3.55}$Mn$_{0.4}$Al$_{0.3}$Co$_{0.75-x}$Fe$_x$ (x = 0, 0.35) compounds before and after electrochemical cycles. *J. Mag. Mag. Mat.* **2002**, *242–245*, 850–853. [CrossRef]

24. Singh, R.K.; Gupta, B.K.; Lototsky, M.V.; Srivastava, O.N. On the synthesis and hydrogenation behavior of MmNi$_{5-x}$Fe$_x$ alloys and computer simulation of their *P–C–T* curves. *J. Alloy. Compd.* **2004**, *373*, 208–213. [CrossRef]

25. Khaldi, C.; Mathlouthi, H.; Lamloumi, J.; Percheron-Guégan, A. Electrochemical impedance spectroscopy and constant potential discharge studies of LaNi$_{3.55}$Mn$_{0.4}$Al$_{0.3}$Co$_{0.75-x}$Fe$_x$ hydrides alloy electrodes. *J. Alloy. Compd.* **2004**, *384*, 249–253. [CrossRef]

26. Singh, R.K.; Gupta, B.K.; Lototsky, M.V.; Srivastava, O.N. Thermodynamical, structural, hydrogen storage properties and simulation studied of P–C isotherms of (La, Mm)Ni$_{5-y}$Fe$_y$. *Int. J. Hydrog. Energy* **2007**, *32*, 2971–2976. [CrossRef]

27. Yang, K.; Liu, X.; Dai, C. Mischmetal-Nickel Hydrogen Storage Material by Adding a Third Element to Control the Plateau Pressure. In *Hydrogen Systems*; Veziroglu, T.N., Zhu, Y., Bao, D., Eds.; Pergamon: New York, NY, USA, 1986; Volume 1, pp. 383–387.

28. Chen, L.; Lei, Y.; Zhu, G.; Wang, Q. The effects of doping Fe to the electrochemical properties of MI(NiCoMnTi)$_5$ metal hydride alloy. *Rare Met. Mater. Eng.* **1998**, *27*, 135–138.

29. Wei, X.; Liu, S.; Dong, H.; Zhang, P.; Liu, Y.; Zhu, J.; Yu, G. Microstructures and electrochemical properties of Co-free AB$_5$-type hydrogen storage alloys through substitution of Ni by Fe. *Electrochim. Acta* **2007**, *52*, 2423–2428. [CrossRef]

30. Yang, H.; Chen, Y.; Tao, M.; Wu, C.; Shao, J.; Deng, G. Low temperature electrochemical properties of LaNi$_{4.6-x}$Mn$_{0.4}$M$_x$ (M = Fe or Co) and effect of oxide layer on EIS response in metal hydride electrodes. *Electrochim. Acta* **2010**, *55*, 648–655. [CrossRef]

31. Liu, B.; Li, A.; Fan, Y.; Hu, M.; Zhang, B. Phase structure and electrochemical properties of La$_{0.7}$Ce$_{0.3}$Ni$_{3.75}$Mn$_{0.35}$Al$_{0.15}$Cu$_{0.75-x}$Fe$_x$ hydrogen storage alloys. *Trans. Nonferrous Met. Soc. China* **2012**, *22*, 2730–2735. [CrossRef]

32. Chao, D.; Zhong, C.; Ma, Z.; Yang, F.; Wu, Y.; Zhu, D.; Wu, C.; Chen, Y. Improvement in high-temperature performance of Co-free high-Fe AB$_5$-type hydrogen storage alloys. *Int. J. Hydrog. Energy* **2012**, *37*, 12375–12383.

33. Kaabi, A.; Khaldi, C.; Lamloumi, J. Thermodynamic and kinetic parameters and high rate discharge-ability of the AB$_5$-type metal hydride anode. *Int. J. Hydrog. Energy* **2016**, *41*, 9914–9923. [CrossRef]

34. Young, K.; Ouchi, T.; Reichman, B.; Koch, J.; Fetcenko, M.A. Improvement in the low-temperature performance of AB$_5$ metal hydride alloys by Fe-addition. *J. Alloy. Compd.* **2011**, *509*, 7611–7617. [CrossRef]

35. Cho, S.; Enoki, H.; Akiba, E. Effect of Fe addition on hydrogen storage characteristics of Ti$_{0.16}$Zr$_{0.05}$Cr$_{0.22}$V$_{0.57}$ alloy. *J. Alloy. Compd.* **2000**, *307*, 304–310. [CrossRef]

36. Young, K.; Nei, J.; Wong, D.F.; Wang, L. Structural, hydrogen storage, and electrochemical properties of Laves phase-related body-centered-cubic solid solution metal hydride alloys. *Int. J. Hydrog. Energy* **2014**, *39*, 21489–21499. [CrossRef]

37. Pan, H.; Li, R.; Liu, Y.; Gao, M.; Miao, H.; Lei, Y.; Wang, Q. Structure and electrochemical properties of the Fe substituted Ti-V-based hydrogen storage alloys. *J. Alloy. Compd.* **2008**, *463*, 189–195. [CrossRef]

38. Dou, T.; Wu, Z.; Mao, J.; Xu, N. Application of commercial ferrovanadium to reduce cost of Ti–V-based BCC phase hydrogen storage alloys. *Mater. Sci. Eng. A* **2008**, *476*, 34–38. [CrossRef]

39. Santos, S.F.; Huot, J. Hydrogen storage in TiCr$_{1.2}$(FeV)$_x$ BCC solid solutions. *J. Alloy. Compd.* **2009**, *472*, 247–251. [CrossRef]

40. Young, K.; Ouchi, T.; Nei, J.; Meng, T. Effects of Cr, Zr, V, Mn, Fe, and Co to the hydride properties of Laves phase-related body-centered-cubic solid solution alloys. *J. Power Sources* **2015**, *281*, 164–172. [CrossRef]

41. Liu, Y.; Cao, Y.; Huang, L.; Gao, M.; Pan, H. Rare earth-Mg-Ni-based hydrogen storage alloys as negative electrode materials for Ni/MH batteries. *J. Alloy. Compd.* **2011**, *509*, 675–686. [CrossRef]

42. Zhang, Y.; Li, B.; Ren, H.; Wu, Z.; Dong, X.; Wang, X. Influences of the substitution of Fe for Ni on structures and electrochemical performances of the as-cast and quenched La$_{0.7}$Mg$_{0.3}$Co$_{0.45}$Ni$_{2.55-x}$Fe$_x$ (x = 0–0.4) electrode alloys. *J. Alloy. Compd.* **2008**, *460*, 414–420. [CrossRef]

43. Wu, F.; Zhang, M.; Mu, D. Effect of B and Fe substitution on structure of AB$_3$-type Co-free hydrogen storage alloy. *Trans. Nonferrous Met. Soc. China* **2010**, *20*, 1885–1891. [CrossRef]

44. Meng, T.; Young, K.; Yasuoka, S. Fe-substitution for Ni in misch metal-based superlattice hydrogen absorbing alloys—Part 2. Performance and failure mechanism in sealed cell. *Batteries* **2016**. to be submitted for publication.

45. Young, K.; Yasuoka, S. Past, Present, and Future of Metal Hydride Alloys in Nickel-Metal Hydride Batteries. In Proceedings of the 14th International Symposium on Metal-Hydrogen Systems, Manchester, UK, 21–25 July 2014.

46. Liu, J.; Han, S.; Li, Y.; Zhang, L.; Zhao, Y.; Yang, S.; Liu, B. Phase structures and electrochemical properties of La–Mg–Ni-based hydrogen storage alloys with superlattice structure. *Int. J. Hydrog. Energy* **2016**. [CrossRef]

47. Young, K.; Ouchi, T.; Fetcenko, M.A. Pressure-composition-temperature hysteresis in C14 Laves phase alloys: Part 1. Simple ternary alloys. *J. Alloy. Compd.* **2009**, *480*, 428–433. [CrossRef]

48. Pourbaix, M. *Atlas of Electrochemical Equilibrium in Aqueous Solutions*; National Association of Corrosion Engineers: Houston, TX, USA, 1974.

49. Li, F.; Young, K.; Ouchi, T.; Fetcenko, M.A. Annealing effects on structural and electrochemical properties of (LaPrNdZr)$_{0.83}$Mg$_{0.17}$(NiCoAlMn)$_{3.3}$ alloy. *J. Alloy. Compd.* **2009**, *471*, 371–377. [CrossRef]

50. Mosavati, N.; Young, K.; Meng, T.; Ng, K.Y.S. Electrochemical open-circuit voltage and pressure-concentration-temperature isotherm comparison for metal hydride alloys. *Batteries* **2016**, *2*. [CrossRef]

51. Young, K.; Ouchi, T.; Meng, T.; Wong, D.F. Studies on the synergetic effects in multi-phase metal hydride alloys. *Batteries* **2016**, *2*. [CrossRef]

52. Young, K. Electrochemical Applications of Metal Hydrides. In *Compendium of Hydrogen Energy*; Barbir, F., Basile, A., Veziroğlu, N., Eds.; Woodhead Publishing Ltd.: Waltham, MA, USA, 2016; Volume 3.

53. Young, K.; Wong, D.F.; Nei, J.; Reichman, B. Electrochemical properties of hypo-stoichiometric Y-doped AB_2 metal hydride alloys at ultra-low temperature. *J. Alloy. Compd.* **2015**, *643*, 17–27. [CrossRef]

54. Young, K.; Ouchi, T.; Nei, J.; Moghe, D. The importance of rare-earth additions in Zr-based AB_2 metal hydride alloys. *Batteries* **2016**, *2*. [CrossRef]

55. Young, K.; Wong, D.F.; Ouchi, T.; Huang, B.; Reichman, B. Effects of La-addition to the structure, hydrogen storage, and electrochemical properties of C14 metal hydride alloys. *Electrochim. Acta* **2015**, *174*, 815–825. [CrossRef]

56. Wong, D.F.; Young, K.; Nei, J.; Wang, L.; Ng, K.Y.S. Effects of Nd-addition on the structural, hydrogen storage, and electrochemical properties of C14 metal hydride alloys. *J. Alloy. Compd.* **2015**, *647*, 507–518. [CrossRef]

57. Stucki, F.; Schlapbach, L. Magnetic properties of $LaNi_5$, FeTi, Mg_2Ni and their hydrides. *J. Less Commun. Met.* **1980**, *74*, 143–151. [CrossRef]

58. Young, K.; Huang, B.; Regmi, R.K.; Lawes, G.; Liu, Y. Comparisons of metallic clusters imbedded in the surface of AB_2, AB_5, and A_2B_7 alloys. *J. Alloy. Compd.* **2010**, *506*, 831–840. [CrossRef]

59. Chang, S.; Young, K.; Ouchi, T.; Meng, T.; Nei, J.; Wu, X. Studies on incorporation of Mg in Zr-based AB_2 metal hydride alloys. *Batteries* **2016**, *2*. [CrossRef]